Modelling lidar volume-averaging and its significance to wind turbine wake measurements

Paper

Meyer Forsting, Alexander Raul; Troldborg, Niels; Borraccino, Antoine

Published in:
Wake Conference 2017

Link to article, DOI:
10.1088/1742-6596/854/1/012014

Publication date:
2017

Document Version
Publisher's PDF, also known as Version of record

Modelling lidar volume-averaging and its significance to wind turbine wake measurements

2017 J. Phys.: Conf. Ser. 854 012014

(http://iopscience.iop.org/1742-6596/854/1/012014)

IOP Conf. Series: Journal of Physics: Conf. Series **854** (2017) 012014 doi:10.1088/1742-6596/854/1/012014

Modelling lidar volume-averaging and its significance to wind turbine wake measurements

A R Meyer Forsting[1], N Troldborg[1], A Borraccino[1]

[1] DTU Wind Energy, Technical University of Denmark, Risø Campus, DK-4000 Roskilde, Denmark

E-mail: alrf@dtu.dk

Abstract. Lidar velocity measurements need to be interpreted differently than conventional in-situ readings. A commonly ignored factor is "volume-averaging", which refers to lidars not sampling in a single, distinct point but along its entire beam length. However, especially in regions with large velocity gradients, like the rotor wake, can it be detrimental. Hence, an efficient algorithm mimicking lidar flow sampling is presented, which considers both pulsed and continous-wave lidar weighting functions. The flow-field around a 2.3 MW turbine is simulated using Detached Eddy Simulation in combination with an actuator line to test the algorithm and investigate the potential impact of volume-averaging. Even with very few points discretising the lidar beam is volume-averaging captured accurately. The difference in a lidar compared to a point measurement is greatest at the wake edges and increases from 30% one rotor diameter (D) downstream of the rotor to 60% at $3D$.

1. Introduction

Lidars rely on the reflection of emitted light from aerosols back to the receiver to measure wind speed. To determine the velocity at the desired measurement location, the beam can be focused (continous-wave) or the backscattered signal split by the time of flight (pulsed). In both cases there are reflections from aerosols away from the desired probe location. Lidars therefore sample the flow velocity all along their beams, albeit with a spatial filter. This is also commonly referred to as "volume-averaging" or "range-weighting". Schematically this is shown in Figure 1 with the weighting function $W(r)$ acting in the local beam coordinate system with $r = |\mathbf{x} - \mathbf{x}_L|$ and peaking at the probe location F. The measured line-of-sight velocity v_{los} at a point in space $\mathbf{x}_F$ is thus given by the convolution of the radial velocities sampled along the beam and the weighting function

$$v_{los}(\mathbf{x}_F) = -\int_0^\infty \mathbf{e}(\mathbf{x}_F, \mathbf{x}_L) \cdot \mathbf{V}(r) W(r)\, \mathrm{d}r \tag{1}$$

Here $\mathbf{e}(\mathbf{x}_F, \mathbf{x}_L)$ represents the beam direction unit vector. The difference between the point and lidar measurement, $\Delta v_r = v_{los} - (-\mathbf{e}(\mathbf{x}_F, \mathbf{x}_L) \cdot \mathbf{V}(\mathbf{x}_F))$, therefore depends on the combination of flow-field and weighting function. This implies that large flow gradients and/or broad weighting functions can lead to significant Δv_r. In wind energy and the atmospheric sciences lidars are becoming ever more popular, especially in model validation, but usually their data are still treated as conventional point measurements. However, with the currently available lidar technology the effect of volume-averaging can be non-negligible, especially in areas of large

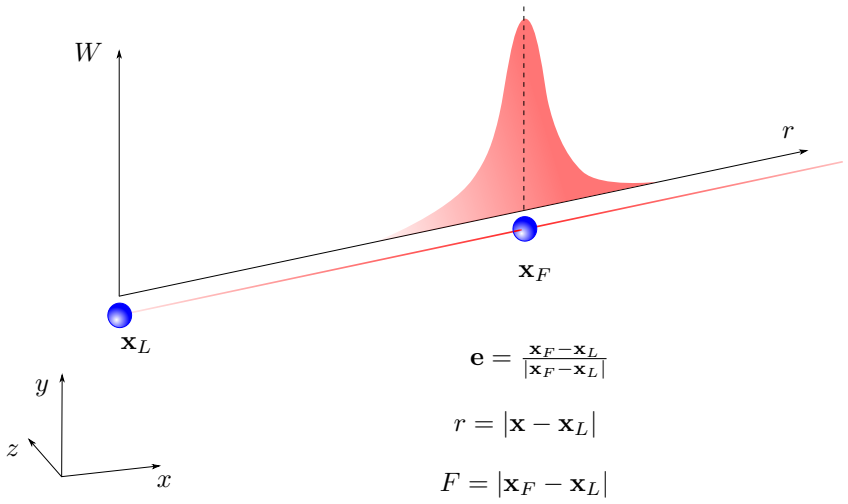

Figure 1. Lidar range weighting of the sampled velocities along the beam. The beam originates from $\mathbf{x}_L$ to measure at $\mathbf{x}_F$. The weighting function acts in the local beam coordinate system.

velocity gradients like the wind turbine wake. Furthermore, continous-wave (CW) and pulsed lidars possess very distinct weighting functions. The large domains of numerically generated flow-fields readily provide $\mathbf{V}(r)$, so only the weighting function remains to be implemented to arrive at a numerical estimate of $v_{los}(\mathbf{x}_F)$. These in turn are valuable to experimentalists using lidars, as they give insight into the magnitude of Δv_r given some measurement setup. This allows optimising the setup and estimating uncertainties, as done by Churchfield *et al.* [1] for a wake experiment with a CW lidar. Simley *et al.* [2] implemented a numerical version of the latter to study the errors from lidar measurements and their implications for feed-forward turbine control. Similarly, Mirocha *et al.* [3] used a virtual pulsed lidar to compare measurements and simulations. Despite presenting the respective weighting functions, there are no details given regarding the actual beam discretisation.

The aim of this paper is to increase the awareness of volume-averaging in lidar measurements, with a focus on wake measurements, and providing a guide for implementing numerical lidars in post-processing. For this purpose computational fluid dynamics (CFD) simulations of the wind turbine wake in flat terrain using an actuator line (AL) are sampled over large regions using numerical, nacelle-based CW and pulsed lidars.

2. Lidar modelling

The fundamental part underlying a numerical implementation of a lidar is the approximation of the weighting function and its efficient discretisation. The former is well established for each respective lidar technology (refer to the references for more detail):

- Continous-wave [4]

$$W_C(r) = \frac{1}{\pi} \frac{z_R}{z_R^2 + (r - F)^2} \quad \text{with} \quad z_R = \frac{\lambda F^2}{\pi \alpha_0^2} \tag{2}$$

- Pulsed [5, 6]

$$W_P(r) = \frac{1}{2\Delta p} \left\{ \mathrm{Erf}\left[\frac{(r - F) + \Delta p/2}{r_p} \right] - \mathrm{Erf}\left[\frac{(r - F) - \Delta p/2}{r_p} \right] \right\}$$
$$\text{with} \quad \mathrm{Erf}(x) = \frac{2}{\sqrt{\pi}} \int_0^x \exp(-t^2)\, \mathrm{d}t \quad \text{and} \quad r_p = \frac{\Delta l}{2\sqrt{\ln(2)}} \tag{3}$$

Here $\lambda, \alpha_0, \Delta p, \Delta l$ are lidar specific constants, usually provided by the manufacturer, and denote laser wavelength, effective telescope radius, range-gate length and lidar beam full width at half maximum, respectively. In figure 2 the influence of these parameters on the lidars' weighting functions are shown. The baseline parameters, which are used throughout the paper, are taken from the ZephIR Dual Mode (CW) and Avent 5-beam Demonstrator (pulsed) (see table 1) and $F = 100$ m. Both functions are symmetric about the probe location F, independent of the choice of parameters. The pulsed weighting function is broader than the one for the continous-wave lidar at this probe location, but it is independent of F. The continous-wave lidar's weighting function on the other hand broadens rapidly with increasing F, as $z_R \propto F^2$. This has some important implications regarding the discretisation of each weighting function, as in a real measurement scenario the only parameter changing is F. Hence, the CW weighting function needs to be re-discretised for each F, whereas the one for a pulsed lidar can be determined once and shifted along r according to F.

Table 1. Lidar parameters used throughout this paper.

CW	α_0	28×10^{-3} m
(ZephIR Dual Mode)	λ	1565×10^{-9} m
Pulsed	Δl	24.75 m
(Avent 5-beam Demo)	Δp	38.4 m

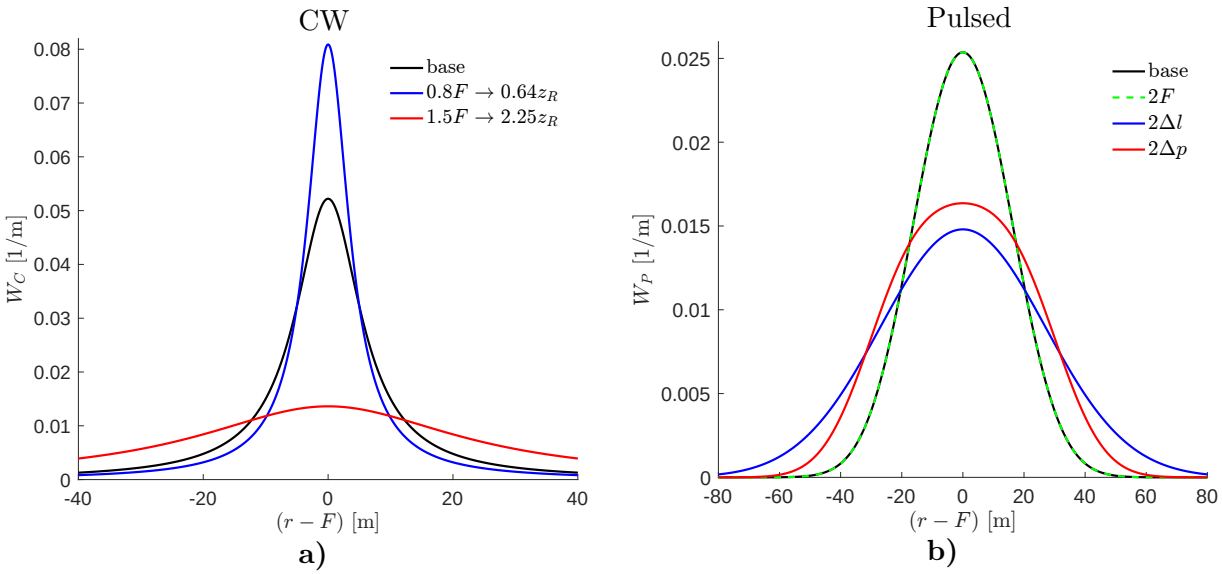

Figure 2. Idealised lidar weighting functions for $F = 100$ m and with baseline parameters given in table 1: a) Continous-wave, equation (2); b) Pulsed, equation (3).

2.1. Discretisation of weighting functions

In discrete space equation (1) becomes

$$v_{los}(\mathbf{x_F}) = \frac{\sum_{i=1}^{n_W} \mathbf{e}(\mathbf{x}_F, \mathbf{x}_L) \cdot \mathbf{V}(r_i) W(r_i)}{\sum_{i=1}^{n_W} W(r_i)} \tag{4}$$

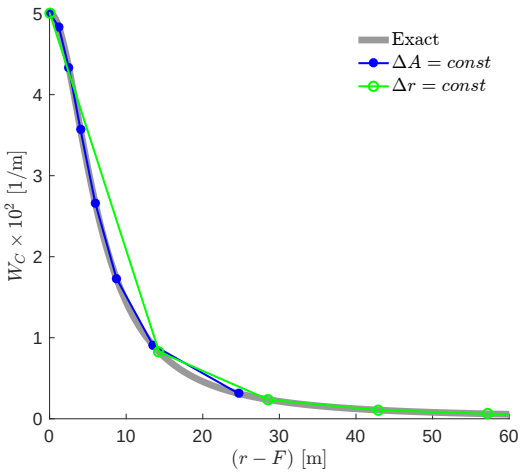

Figure 3. Continous-wave lidar weighting function as defined in equation (2) with $F = 100$ and discretised with either linear spacing in ΔA or Δr each with $n_W = 15$. Lidar parameters: $\lambda = 1565 \times 10^{-9}$ m; $\alpha_0 = 28 \times 10^{-3}$ m.

where n_W denotes the number of points used to discretise the lidar beam. It is directly linked to the numerical efficiency of estimating $v_{los}(\mathbf{x}_F)$, as it determines the number of locations at which $\mathbf{V}$ needs to be evaluated by some costly interpolation. Using a linear point distribution in r the convergence of v_{los} is poor, as the functions are not sampled sufficiently in regions where W is large. Instead, the the area under the curve should be conserved to preserve the shape of the function as shown in Figure 2.1 for $n_W = 15$. Adopting this strategy the integral of the respective weighting function needs to be determined:

$$\Delta A = \int_{r_i}^{r_{i+1}} W(r)\,\mathrm{d}r = const \tag{5}$$

with

$$\Delta A = \frac{2A_F}{(n_W - 1)} \quad \text{and} \quad A_F = \int_{-\infty}^{F} W(r)\,\mathrm{d}r \tag{6}$$

Here the symmetry of the weighting functions is used. The discretisation approach of each function differs, due to the nature $\int W(r)$.

2.1.1. Continous-wave Equation (2) has a definite integral

$$\Delta A = \int_{r_i}^{r_{i+1}} W_C(r)\,\mathrm{d}r = \frac{1}{\pi}\left[\tan^{-1}\left(\frac{r-F}{z_R}\right)\right]_{r_i}^{r_{i+1}} \tag{7}$$

It follows that

$$A_F = \int_{0}^{F} W_C(r)\,\mathrm{d}r = \frac{1}{\pi}\tan^{-1}\left(\frac{F}{z_R}\right) \tag{8}$$

Here the lower bound is set to zero instead, as $\int_{-\infty}^{0} W_C(r)\,\mathrm{d}r \approx 0$. By rearranging equation (7) the point distribution can be determined

$$r_{i+1} = z_R \tan\left(\tan^{-1}\left(\frac{r_i - F}{z_R}\right) - \Delta A\pi\right) + F \tag{9}$$

The best starting location is $r_1 = F$ and the sampling points only need to be evaluated for one side and reflected in $r - F$.

2.1.2. Pulsed The error function has no definite integral, requiring a numerical approach. As W_P is independent of F, the discretisation should be performed only once for $s = r - F$. The shape of the weighting function requires choosing a certain cut-off value $w_{\min}$ until which the weighting function is discretised. The corresponding point $s_{\min}$ can be determined numerically down to a certain tolerance. Consequently s can be discretised linearly with a high resolution in the region $0 \leq s \leq s_{\min}$ to evaluate $\mathbf{w}^+ = W_P(\mathbf{s}^+)$. Some quadrature rule can then be used to determine $\mathbf{A}^+(\mathbf{s}^+)$, which is summed to determine A_F and consequently ΔA (see equation 6). Lowering the level of discretisation reduces computational time as less interpolation is performed in the flow domain. The final discretised weighting function should be sampled at each s_i corresponding to an area $i\Delta A$, which can be interpolated from $\mathbf{A}^+(\mathbf{s}^+)$. Reflecting $\mathbf{w}(\mathbf{s})$ in 0 gives the fully discretised W_P and to recover the beam coordinate system $\mathbf{r} = \mathbf{s} + F$.

2.2. Domain boundary exceeding beams
Depending on the probe location and the beam direction, some part of the lidar beam may lie outside the computational domain. Additionally, pulsed lidars give weight to velocities sampled at $r < 0$, when $F < 2\Delta l$. One solution to obtain an estimate of v_{los}, despite missing parts of the weighting function, is to scale the weights with regard to the total inside the domain

$$\tilde{W}(r) = \frac{W(r)}{\int_0^{r_\Omega} W(r)\,\mathrm{d}r} \tag{10}$$

Here r_Ω denotes the intersection of the beam with the domain boundaries. In a real measurement scenario it is not unusual that $\int_0^{r_\Omega} W(r)\,\mathrm{d}r \neq 1$, which corresponds to a beam intersecting hard targets like towers, turbines, ground etc. Usually these measurements are outright rejected by the lidar signal processing software, as hard targets show up as anomalies in the Doppler spectra. Similarly, a pulsed lidar cannot measure at around $F < 2\Delta l$ for technical reasons (internal reflections etc. [7]). Therefore numerical estimates of v_{los} for which $\int_0^{r_\Omega} W(r)\,\mathrm{d}r < 1$ should be treated with caution.

3. Computational method

3.1. Flow solver and modelling approach
The finite-volume solver, EllipSys3D, discretises the Navier-Stokes equations over a block-structured domain [8–10]. The SIMPLE algorithm [11] solves the pressure-linked terms of the Navier-Stokes equations and a modified Rhie-Chow algorithm the pressure equation [12]. Time-stepping is achieved through an iterative, second-order scheme. The turbulence is either modelled by a Reynolds-averaged Navier-Stokes (RANS) formulation with a Menter k–ω shear-stress transport closure [13] or by solving the filtered Navier-Stokes equations with a sub-grid scale (SGS) model by Ta Phouc [14]. Switching between models is determined by a limiter function as defined by Strelets [15]. This also determines whether the QUICK [16] (RANS) or a fourth-order CDS scheme (LES) discretises the convective terms. The rotor forces are introduced by an actuator line [17, 18].

3.2. Siemens SWT 2.3-93

The turbine is a commercial product by Siemens Wind Power with a rated power of 2.3 MW and a three-bladed rotor with 93 m diameter. The hub is located 80 m above. At a hub height wind speed of 8 m/s it performs 15 rotations per minute and $C_T = 0.81$.

3.3. Numerical domain

A box domain with 25 radii (R) side length reduces the blockage from the turbine ($\pi/25^2 = 0.5\%$). The bottom boundary is a no-slip wall and the top, side and rear boundary conditions follow the shear profile (Dirichlet). The AL is located centrally, at a hub height of 80 m, and is surrounded by a finely meshed box with 2.5 R side length and a grid spacing of $R/32$. This resolution is sufficient for accurate wake simulations using an AL [19, 20]. The wall cell of the structured mesh is set to 0.05 m and grows [8] hyperbolically in the vertical direction until reaching the equispaced finely meshed box. From there the mesh spacing increases hyperbolically towards the outer domain edges.

3.4. Numerical setup

The hub height velocity was 8 m/s and the inflow profile followed the power law with an exponent of 0.3. The kinematic viscosity and air density were set to 1.789 $\times 10^{-5}$ kg/m/s and 1.225 kg/m^3, respectively. Neither nacelle nor tower were modelled. The smearing factor of the AL is set to twice the grid spacing as suggested by Troldborg *et al.* [19].

The flow was sampled with a CW and pulsed lidar situated at the rotor centre. The parameters of the lidars were those given in table 1. The probe locations $\mathbf{x}_F$ lay in a vertical ($x - z$) and horizontal ($x - y$) plane passing through the rotor centre. The spacing between probe locations was $D/50$ in both directions.

4. Results

4.1. The mean flow-field

The developing mean flow-field is shown in Figure 4. The large C_T of 0.81 induces strong velocity gradients and peak deficit. The wake is asymmetric, due to the interaction of shear with wake rotation. The rotor blocks the incoming flow, leading to deceleration in the wall-bound regions upstream and re-acceleration downstream. This flow-field presents a challenging test case for lidars with its large velocity gradients.

4.2. Beam discretisation & v_{los} convergence

The convergence of the line-of-sight velocity Δv_{los} with respect to the number of points discretising the lidar beam is investigated over the region outlined in Section 3.4. Here the residual error is defined as

$$\epsilon^i = \frac{v_{los}^i - v_{los}^{i\text{-}1}}{v_{los}^{i\text{-}1}} \tag{11}$$

with i representing the discretisation level. For the vertical plane sampled by a CW lidar and $n_W = 19$ the residuals are shown in Figure 5. Only probe locations where the entire beam lies inside the domain ($\int_0^{r_\Omega} W(r)\,\mathrm{d}r = 1$) are presented. Close to the rotor v_{los} has converged further than downstream in the wake. This is linked to the CW lidar's weighting function: it is very acute close to the rotor but stretches quickly, necessitating more points for an accurate representation. Furthermore, close to large velocity gradients, as at the wake edge, the exact point distribution starts to play an important role. Figure 6 summarises the change of the v_{los} residual with n_W over the vertical plane for both lidars. Convergence is of second order for the CW and nearly third order for the pulsed lidar. Therefore even with few points discretising the beam the effect of volume-averaging can be captured. Note that beyond $n_W > 100$ the beam

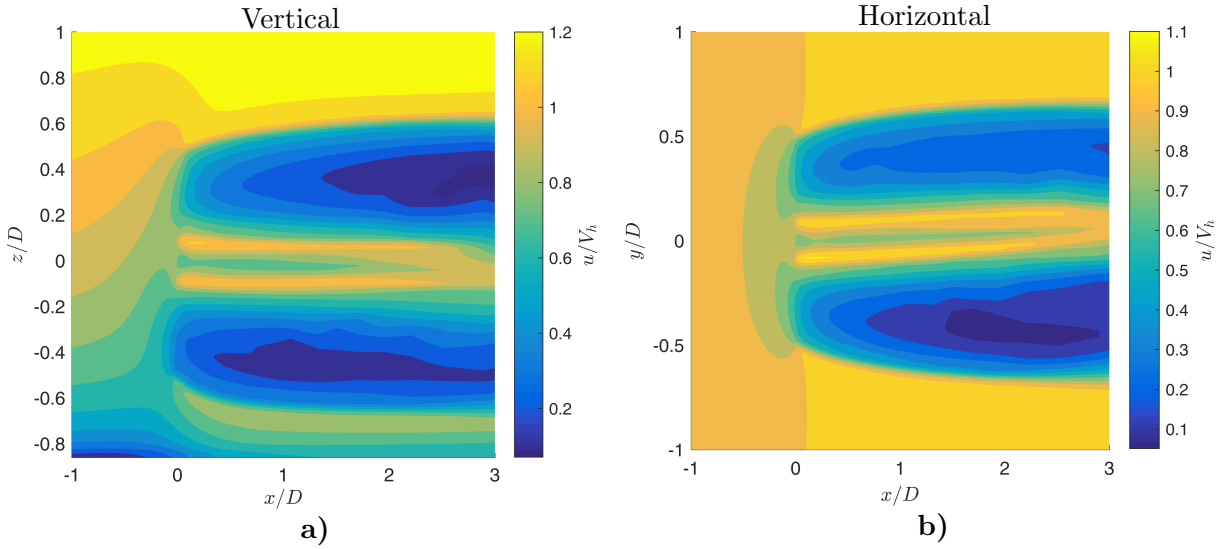

Figure 4. Contours of the time-averaged streamwise velocity component normalised by the hub height velocity $V_h = 8$ m/s in the a) vertical b) horizontal plane through the rotor centre.

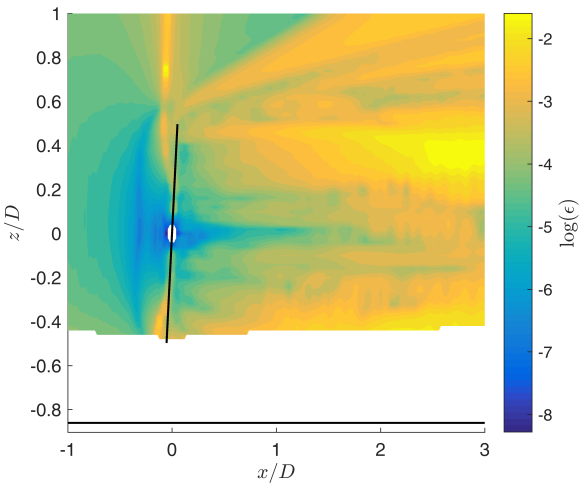

Figure 5. Contours of the v_{los} residual for the CW lidar with $n_W = 19$ discretising the beam. Regions where $\int_0^{r_\Omega} W(r)\,\mathrm{d}r \neq 1$ are removed.

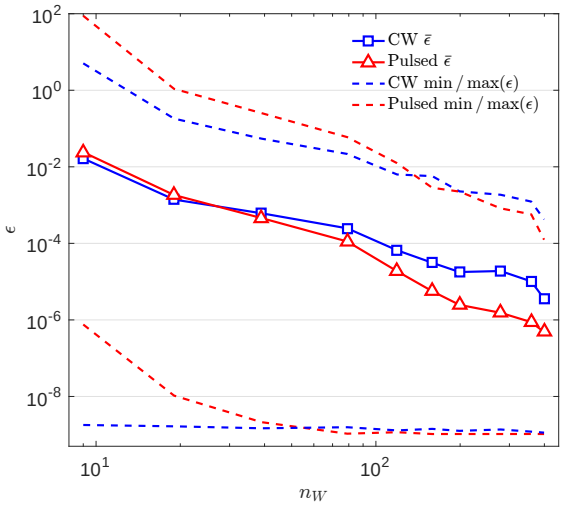

Figure 6. Evolution of the line-of-sight velocity v_{los} residual with number of beam points n_W. Mean and extreme values are determined over a vertical plane ($-3 \leq x/D \leq 3, y/D = 0, -0.86 \leq z/D \leq 1$).

discretisation becomes finer than that of the flow-field and the residuals continue to fall due to interpolation in the flow domain.

4.3. The effect of volume-averaging

To investigate the effect of volume-averaging the flow-field sampled by lidars are compared to point-like measurements, such that

$$\Delta\tilde{v}_{los} = \frac{v_{los}^{\text{lidar}} - v_{los}^{\text{point}}}{v_{los}^{\text{point}}} \tag{12}$$

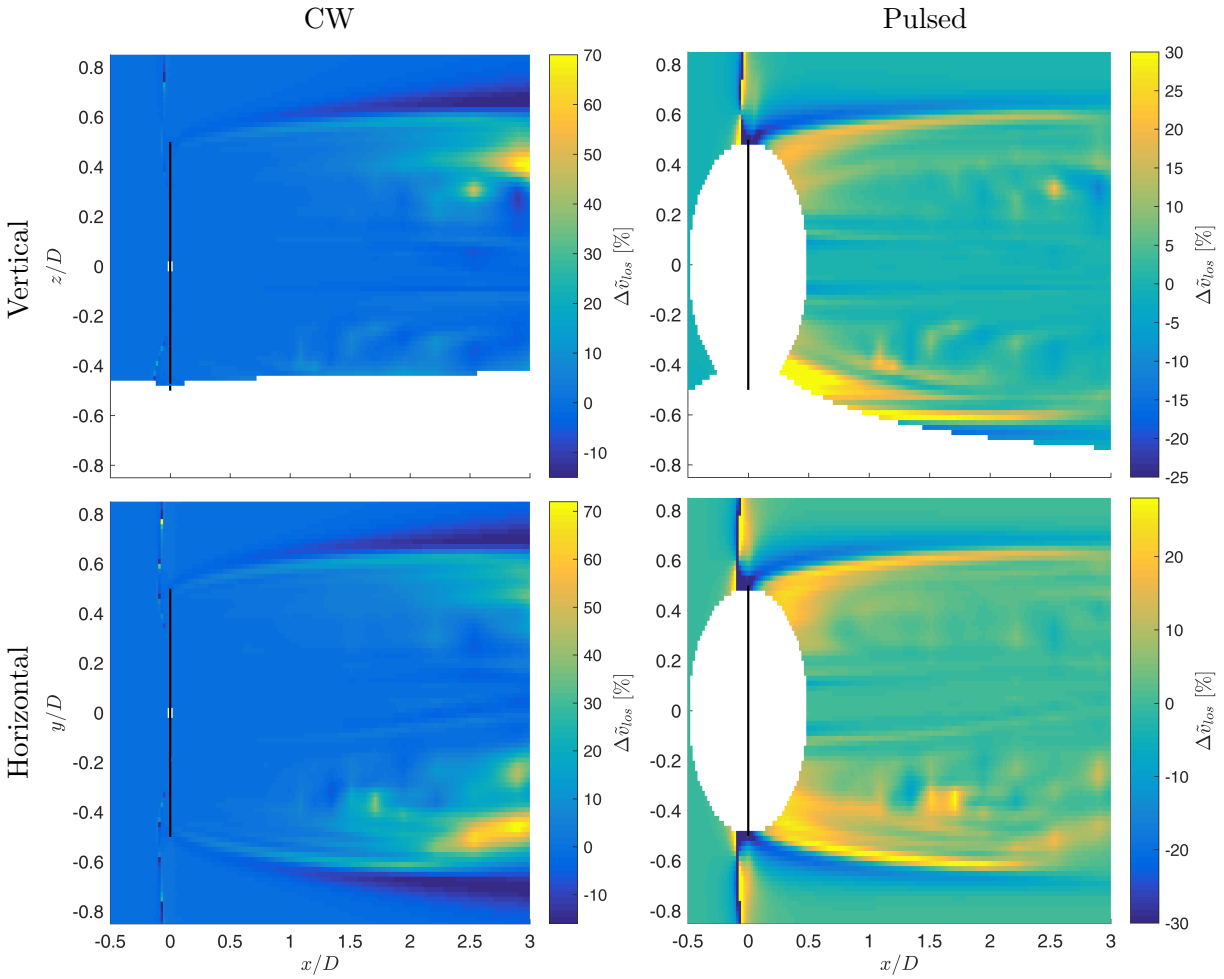

Figure 7. Time-averaged relative difference in the line-of-sight velocity $\Delta\tilde{v}_{los}$ measured by a CW (left) and pulsed (right) in a vertical (top) and horizontal plane (bottom) with respect to point-like velocities.

Time-averaged contours of this quantity are shown in Figure 7 for both planes and lidars. Note that here the beam was discretised with $n_W = 200$ and again probe locations where $\int_0^{r_\Omega} W(r)\,\mathrm{d}r \neq 1$ are excluded. Unsurprisingly, for both lidars the difference to point-like measurements are most prominent around the wake edges, due to the large velocity gradients. However, whereas the CW sampled velocities present nearly no volume-averaging close to the rotor, the pulsed system suffers greatest in this region. The inverse is true the further the probe locations move downstream. This is clearly related to the CW lidar's weighting function spreading quickly with F^2. The pulsed lidar's weights are unchanged with distance, but close to the rotor the beam cuts the wake edge nearly orthogonally.

This results in a relatively small v_{los} and in combination with sampling along a large velocity gradient introduces substantial amounts of volume-averaging. The large difference encountered in the rotor plane also stems from sampling the flow perpendicular to the mean flow direction. To give a more quantitative impression of volume-averaging in the wake, Figure 8 compares the difference in the line-of-sight velocities at different longitudinal stations between lidars. Upstream the velocity profile is nearly unchanged, except close to the ground, whereas in the wake there are significant alterations, mostly leading to larger measured velocities. This is most prominent around the wake edges.

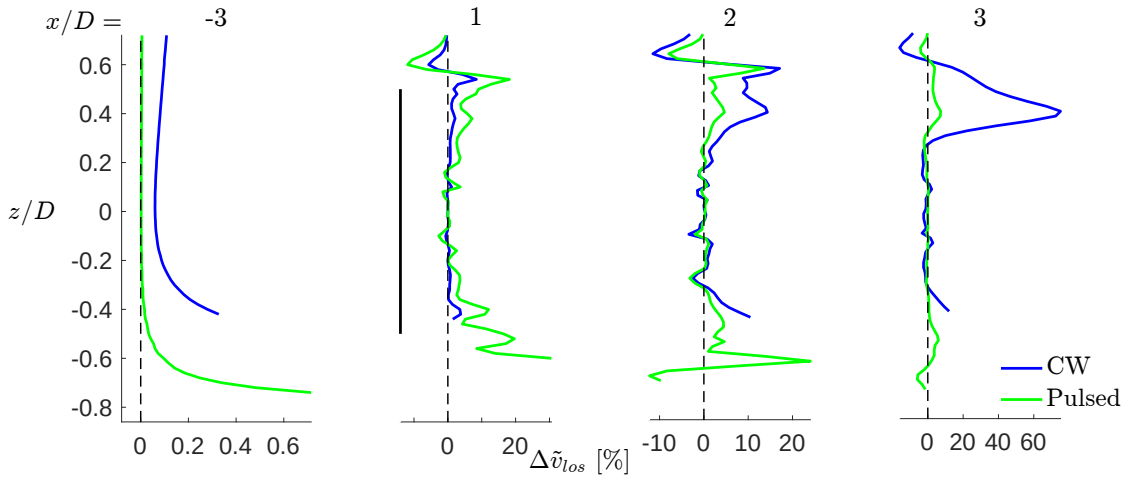

Figure 8. Time-averaged difference in the measured line-of-sight to point-like velocities along z at changing locations along the centreline.

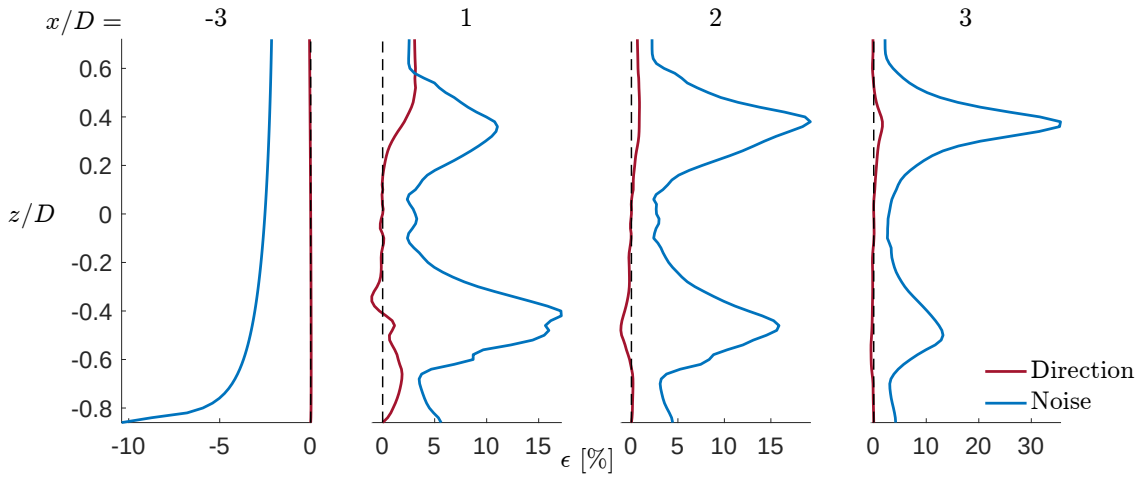

Figure 9. Directional and noise errors (only positive) along the same lines as Figure 8.

However, as discussed by Simley *et al.* [21], there are various other errors impacting lidar measurements, namely directional bias, signal noise and flow evolution. Here the directional bias refers to the error incurred by estimating the streamwise velocity from line-of-sight measurements ("cyclops dilemma"). Random measurement noise is unavoidable and introduces uncertainty in the measured velocities by disturbing the Doppler spectra. Both errors were computed for the transects already shown in Figure 8 following the definition of Simley *et al.*, which assumes a maximum noise error of $\pm$ 0.2 m/s. They are presented in Figure 9, which highlights that signal noise is the more significant of both. Referring to Figure 8, noise plays a detrimental role with respect to the total error, as it is of the same magnitude as the volume-averaging effect. Upstream it is in fact the only significant error source. Nevertheless, it should be kept in mind that the noise level needs to be reassessed for each measurement campaign, as it can vary significantly [21]. Therefore, the impact from noise presented here cannot be generalised.

5. Conclusion

Lidar volume-averaging can be readily implemented in existing flow simulation tools, as it is solely an additional post-processing step. An efficient and accurate method for discretising the lidar beam weighting function is presented, that allows lidar sampling at each time step at limited computational cost. Wake measurements are affected by volume-averaging especially at the wake edges, due to the large velocity gradients being smeared out. However the type of lidar, CW or pulsed, determines the region in which it is most prominent: close to the rotor the CW shows nearly none, whereas the pulsed lidar's velocity might reach 30% of a point-like measurement; the opposite is true beyond 200 m downstream. The lidar measurement location and type therefore determine whether volume-averaging should be incorporated into simulation data post-processing. As there are many variables determining the lidar line-of-sight velocity it is, however, hard to make a general statement regarding the significance of volume-averaging.

Acknowledgments

This work was performed inside the UniTTe project (unitte.dk), which is financed by The Innovation Fund Denmark, grant number 1305-00024B. Computational resources were provided by the Risø DTU central computing facility. Furthermore, we would like to thank Siemens Wind Power and the lidar manufacturers ZephIR and Avent.

References

[1] Churchfield M, Wang Q, Scholbrock A, Herges T, Mikkelsen T and Sjöholm M 2016 *Journal of Physics: Conference Series* **753**
[2] Simley E, Pao L Y, Frehlich R, Jonkman B and Kelley N 2012 Analysis of wind speed measurements using continous wave lidar for wind turbine control *49th AIAA Aerospace Sciences Meeting* AIAA 2011-263 (Orlando, Flordia, US)
[3] Mirocha J D, Rajewski D A, Marjanovic N, Lundquist J K, Kosovic B, Draxl C and Churchfield M J 2016 *Journal of Physics: Conference Series* **753**
[4] Sonnenschein C M and Horrigan F A 1971 *Applied Optics* **10**
[5] Banakh V A and Smalikho I N 1997 *Atmos. Oceanic Opt.* **10** 957–965
[6] Sonnenschein C M and Horrigan F A 1997 *J. Atmos. Oceanic Technol.* **14** 54–75
[7] Vasiljevic N, Courtney M and Mann J 2014 *A time-space synchronization of coherent Doppler scanning lidars for 3D measurements of wind fields* Ph.D. thesis DTU Wind Energy
[8] Sørensen N 1995 *General purpose flow solver applied to flow over hills* Ph.D. thesis Risø National Laboratory
[9] Michelsen J 1994 Basis3d - a platform for development of multiblock pde solvers Tech. rep. Dept. of Fluid Mechanics, Technical University of Denmark, DTU
[10] Michelsen J 1994 Block structured multigrid solution of 2d and 3d elliptic pdes Tech. rep. Dept. of Fluid Mechanics, Technical University of Denmark, DTU
[11] Patanker S and Spalding D 1972 *International Journal of Heat and Mass Transfer*
[12] Réthoré P E and Sørensen N 2012 *Wind Energy* **15** 915–926
[13] Menter F R 1993 *AIAA Journal*
[14] Phouc T 1994 *Modèles de sous maille appliqués aux écoulmements instationnaires décollés* (LIMSI)
[15] Strelets M 2001 Detached eddy simulation of massively separated flows 39th *AIAA Aerospace Sciences Meeting and Exhibit* AIAA Paper 2001-0879 (Reno,NV)
[16] Leonard B 1979 *Computer Methods in Applied Mechanics and Engineering* **19** 59–98
[17] Srensen J N and Shen W Z 2002 *Journal of Fluids Engineering* **124** 393–399
[18] Mikkelsen R 2003 *Actuator Disc Methods Applied to Wind Turbines* Ph.D. thesis Technical University of Denmark
[19] Troldborg N, Sørensen J and Mikkelsen R 2009 *Actuator Line Modeling of Wind Turbine Wakes* Ph.D. thesis Technical University of Denmark
[20] Meyer Forsting A and Troldborg N 2015 *Journal of Physics: Conference Series (Online)* **625** ISSN 1742-6596
[21] Simley E, Pao L Y, Frehlich R, Jonkman B and Kelley N 2014 *Wind Energy* **17** 413–433